Journal of Materials Chemistry A

ROYAL SOCIETY OF CHEMISTRY

PAPER

View Article Online
View Journal | View Issue

Cite this: J. Mater. Chem. A, 2024, 12, 26627

Ultrafast degradation of organic pollutants enabled by nanofluidic ZIF-67/GO membranes *via* efficient nanoconfined peroxymonosulfate activation†

Jian Hu,[a] Jue Hou,[a] Chen Zhao,[a] Yuyu Su,[a] Rong Wang[b] and Huacheng Zhang*[a]

Peroxymonosulfate (PMS)-based advanced oxidation processes are often suggested as a solution for degrading persistent organic pollutants in water. However, despite significant efforts to increase PMS activator catalytic activity, the low yield and short lifespan of reactive radicals present a challenge to their practical application in wastewater treatment, particularly under alkaline conditions. To address this, we have developed nanofluidic zeolite imidazolate framework-67 (ZIF-67)/graphene oxide (GO) membranes for confined PMS activation to remove bisphenol A (BPA) and other organic pollutants from wastewater. The membrane achieves a 100% degradation efficiency of the pollutants at high water fluxes of up to 875 L m^{-2} h^{-1} bar^{-1}, with a superfast reaction rate constant (39 000 min^{-1}) over all previously reported membrane-based catalyst systems. Quenching experiments and chemical probes confirm that both hydroxyl radicals ($^{\bullet}OH$) and sulfate radicals ($SO_4^{\bullet-}$) play dominant roles in the degradation of organic pollutants, as supported by electrochemical characterization. The hybrid porous structure of the ZIF-67/GO membrane consisting of 2D nanochannels between ZIF-67/GO nanosheets and intrinsic ZIF-67 nanopores could offer adjacent pathways for efficient PMS activation and ultrafast BPA degradation. Our findings provide new insight into designing alkaline PMS activators and pave the way for nanoconfinement catalysis in water purification.

Received 8th April 2024
Accepted 18th July 2024

DOI: 10.1039/d4ta02401j

rsc.li/materials-a

Introduction

Peroxymonosulfate (PMS)-based advanced oxidation processes (AOPs) have emerged as a promising strategy for removing refractory organic pollutants from wastewater due to their strong oxidizing ability, high stability, wide pH ranges, and ease of transportation and storage.[1] Generally, appropriate PMS activators have been explored to generate reactive oxygen species (ROSs) to oxidize organic pollutants *in situ*,[2,3] with homogeneous activators being used less frequently than heterogeneous ones. The latter are widely used in wastewater treatment due to their long-term stability, strong oxidizing ability, ease of separation, *etc.*[4,5] However, most of these activators still suffer from the lack of active sites and poor electron transfer properties.[6] Moreover, most PMS activators can only function optimally at pH levels ranging between 3 and 9.[7–10] Sporadic studies focus on alkaline wastewater treatment by activating PMS.

Employing nanoconfinement effects in PMS-based AOPs has received significant attention due to their ability to encapsulate short-lived ROSs and target pollutants in a nanoscale environment, which dramatically enhances the mass transfer efficiency and catalytic performance.[11] Compared to the conventional heterogeneous metal- or carbon-based catalysts,[12–15] metal–organic frameworks (MOFs) membranes have been increasingly focused on by more researchers as PMS activators for wastewater treatment, due to their flexible skeletons, regular porosity, high pore volume, and other advantages.[16] Li *et al.*[17] fabricated bimetallic CuCo-MOF-74 for methylene blue removal and found that the highest efficiency of PMS decomposition was realized with a Cu/Co ratio of 1 : 1. Mei *et al.*[18] employed iron-based MIL-53(Fe) MOFs as the PMS activator and obtained a rate constant of 0.17561 min^{-1} in rhodamine B degradation. However, the mechanical strength and the risk of secondary contamination caused by metal leaching inevitably limited their utilization in further applications.

The zeolite imidazolate framework (ZIF), as a typical member of the MOF family, has been widely studied in various fields, such as photocatalysis,[19] gas separation,[16] adsorption,[20] ion separation,[21] *etc.* due to its large pore volumes, high specific area, and superior thermal and chemical stability. However, most ZIF-derived nanoparticles struggle to form a continuous and complete framework, leading to weak electronic

[a]Chemical and Environmental Engineering, School of Engineering, RMIT University, Melbourne, VIC 3000, Australia. E-mail: huacheng.zhang@rmit.edu.au
[b]School of Civil and Environmental Engineering, Nanyang Technological University, 50 Nanyang Avenue, 639798, Singapore

† Electronic supplementary information (ESI) available. See DOI: https://doi.org/10.1039/d4ta02401j

conductivity for catalysis.[22] Two-dimensional (2D) materials with an atomic-level thickness and a large specific surface area, such as graphene oxide (GO), provide a considerable platform for metal dispersion and promote membrane-confined heterogeneous catalysis.[23] Mona *et al.*[24] loaded Ag nanoparticles on ZIF-67 covered by GO, realizing 100% phenol degradation in 30 min and total *E. coli* inactivation in 15 min through PMS activation. Lin *et al.*[25] synthesized a bulk magnetic cobalt-graphene nanocomposite *via* carbonizing a mixture of ZIF-67 nanoparticles and GO nanosheets for PMS activation with stirring in the solution, achieving a kinetic rate of 0.0119 min^{-1} for the decolorization of Acid Yellow. Despite these findings, there are still scarce reports on the nanoconfinement created from the integration of ZIF-67 and GO towards efficient PMS activation under alkaline conditions.

Herein, a nanofluidic membrane of a hybrid material composed of ZIF-67 and GO was fabricated by filtering ZIF-67/GO nanosheets onto a porous polyethersulfone (PES) membrane (Fig. 1a). ZIF-67/GO nanosheets were synthesized by growing ZIF-67 nanocrystals onto the surface of GO nanosheets. The resulting hybrid membrane reactor provided a nanoconfined platform for PMS activation in pollutant degradation (Fig. 1b and c). Bisphenol A (BPA), an endocrine disruptor and plastic additive commonly found in aquatic systems, was selected as the target pollutant. The nanofluidic ZIF-67/GO membranes of 1.4 μm in thickness could achieve ultrafast degradation of BPA at a high-water flux of 875 L m^{-2} h^{-1} bar^{-1}. The membrane exhibited a 100% removal efficiency for BPA and five other organic pollutants, with a reaction rate constant of approximately 39 000 min^{-1}, seven orders higher than that of bulk non-confined ZIF-67/GO nanosheets. In addition, the performance of the nanofluidic ZIF-67/GO membrane surpassed those of previously reported membrane-based AOP systems 5- to 10 000-fold (Table S1†). This study provides a new strategy for treating alkaline wastewater, shedding new light on fabricating nanoconfined fluids and improving ROS yields.

Results and discussion

Microanalysis and characterization of the ZIF-67/GO membrane

The hybrid ZIF-67/GO membranes were prepared by coating GO nanosheets with ZIF-67 nanoparticles and subsequently assembling them onto a PES substrate (mean pore size of 0.03 μm in Fig. S1†) through a filtration approach (Fig. 1d). The GO dispersion was introduced into the precursors containing coordination metals (Co^{2+}) and imidazole organic ligands (Hmim) under standard atmospheric pressure and at room temperature. ZIF-67 nanocrystals grew on both sides of GO nanosheets, forming a sandwich-like morphology of ZIF-67/GO/ZIF-67 (Fig. 1e and f). From the scanning electron microscopy (SEM) image (Fig. 1g), the surface of the ZIF-67/GO hybrid membrane was relatively smooth with no pinholes or cracks. The particle size of ZIF-67 in ZIF-67/GO showed almost no

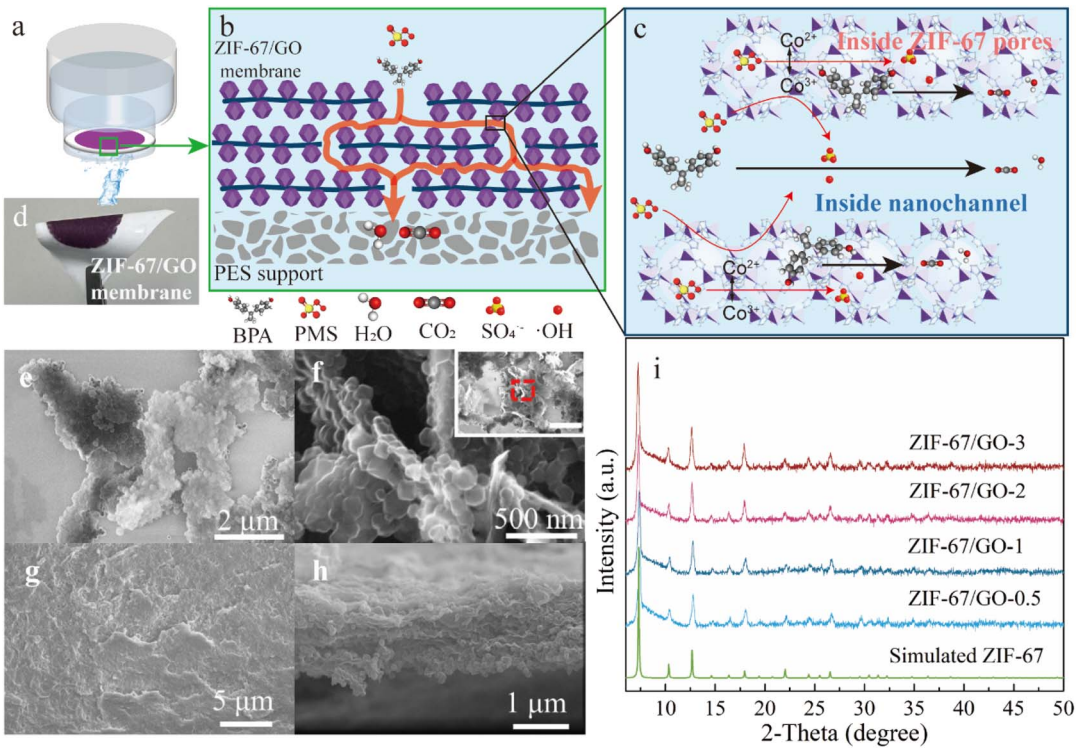

Fig. 1 (a–c) Schematic illustration of the ZIF-67/GO hybrid membrane for the BPA removal in wastewater. (d) Photograph of the flexible ZIF-67/GO membrane on a PES support. (e and f) SEM images of the surface and cross section of the ZIF-67/GO-3 nanosheets. (g) SEM image of the ZIF-67/GO-3 hybrid membrane surface. (h) SEM images of the cross-sectional view of the ZIF-67/GO-3 membrane. (i) XRD patterns of ZIF-67/GO-0.5, ZIF-67/GO-1, ZIF-67/GO-2, ZIF-67/GO-3, and the simulated ZIF-67 structure.

change compared to the ZIF-67 particles alone (Fig. S2a†). The cross-section of the hybrid ZIF-67/GO membrane, with a thickness of around 1.38 μm (Fig. 1h), exhibited a distinct laminated structure, preserving active surfaces or edges compared to the pristine 2D structure. Meanwhile, the 2D hybrid nanosheets created a 2D nanoconfined space, forming abundant nanochannels inside the interspacing.[26]

ZIF-67/GO nanosheets with different synthesis times (0.5 h, 1 h, 2 h, and 3 h) were prepared and denoted as ZIF-67/GO-0.5, ZIF-67/GO-1, ZIF-67/GO-2 and ZIF-67/GO-3, respectively (Fig. S2a†). With a longer synthesis time, the ZIF-67 nanoparticles gradually grew more densely on the surface of GO (Fig. S2 and S3†), potentially providing more active sites for catalysis and higher possibilities for electron transfer. X-ray diffraction (XRD) patterns (Fig. 1i) of these materials showed a high degree of crystallinity with a pure ZIF-67 phase, evidenced by comparing with the pattern of the simulated ZIF-67. Peak intensities were quite similar with the increasing synthesis time, indicating the fast crystallization speed of ZIF-67. Meanwhile, as shown in the XPS survey spectra (Fig. S3†), the existence of Co 2p, O 1s, C 1s, and N 1s confirmed the successful synthesis of ZIF-67/GO composites as well.

Catalytic performance and stability

To illustrate the catalytic performance of the nanoconfined environment, ZIF-67 and ZIF-67/GO-3 were first compared in terms of BPA oxidation. According to the BET result (Fig. S4a†), although the surface area of ZIF-67 (1627.4 $m^2 g^{-1}$) was nearly twice as much as that of ZIF-67/GO-3 (840.4 $m^2 g^{-1}$), the ZIF-67/GO-3 membrane/PMS system exhibited excellent BPA removal efficiency of 100%, significantly outperforming the ZIF-67 membrane/PMS system (48%) (Fig. S4b†). Fig. S4c† compared a plausible pathway of BPA molecules in both systems. For the bulk state of the ZIF-67 membrane system, the BPA molecules preferred to pass through the membrane in the easiest and fastest way with less resistance, leading to fewer opportunities to contact the active sites. In other words, the nanoconfined environment in the laminar ZIF-67/GO-3 structure provided the pollutant molecules more opportunities and higher possibilities to contact with the active sites compared to the bulk state. Hence, the catalytic performance of the ZIF-67/GO-3 membrane was much higher than that of the ZIF-67 membrane. Furthermore, the EIS results in Fig. S4d† indicated that ZIF-67/GO-3, with a smaller semicircle diameter than ZIF-67, benefited from the presence of GO, not only supporting a laminar structure for ZIF-67 particles but also reducing the electron transfer resistance. GO facilitated charge transfer during the oxidation process, which accelerated the rate-limiting step of the cobalt redox reaction,[27] revealing stronger electron transfer ability and providing better catalytic performance for ZIF-67/GO-3. As illustrated above, designing the ZIF-67/GO-3 membrane with a spatial nanoconfined environment could significantly promote the catalytic performance.

The degradation of BPA was also systematically studied to investigate the catalytic performance using ZIF-67/GO-*x* materials as PMS activators. First, to balance the catalytic performance and permeance, the thickness and area sizes of the ZIF-67/GO-3 membrane were optimized. Fig. S5a† shows that the catalytic performance improved, but the water flux dropped with the increase in the membrane thickness. 100% BPA degradation efficiency could be realized at a membrane thickness of ≥1.38 μm. Hence, 1.38 μm membrane thickness was selected with 100% BPA removal efficiency and 875 L m^{-2} h^{-1} bar^{-1} performance for the following studies. The BPA removal efficiency and water flux are similar as the membrane diameter increases from 13 to 37 mm (Fig. S5a†). So a diameter of 13 mm was selected for the following studies. Furthermore, as shown in Fig. 2a, single ZIF-67/GO-3 membrane adsorption played negligible roles in BPA removal with only ~6.2% removal efficiency, indicating limited effectiveness of molecular sieving and adsorption mechanisms. PMS alone also exhibited very poor BPA removal performance (~2.1%) due to the insufficient generation of active radicals through self-decomposition.[28] However, an obvious increase in BPA removal efficiency could be achieved with the simultaneous presence of ZIF-67/GO-3 nanosheets and PMS, which reached 92.3% within 100 min. This indicated that the ZIF-67/GO-3 nanosheets were able to effectively activate PMS for BPA removal. In addition, when compared to the same amount of bulk ZIF-67/GO-3 nanosheets, the ZIF-67/GO-3 membrane/PMS system exhibited much higher oxidation efficiency with 100% BPA degraded in only 7.0 ms, which was also faster than traditional AOPs. The first-order rate constant of the BPA removal process was 39 000 min^{-1} (0.65 ms^{-1}, inset of Fig. 2b), which was around 7 orders of magnitude higher than that of the non-confined heterogenous ZIF-67/GO nanosheets (0.025 min^{-1}, Fig. S6†). It was also up to 7 orders of magnitude higher than those of other membrane-based catalytic systems (0.11–7866 min^{-1}, Fig. 2c and Table S1†).

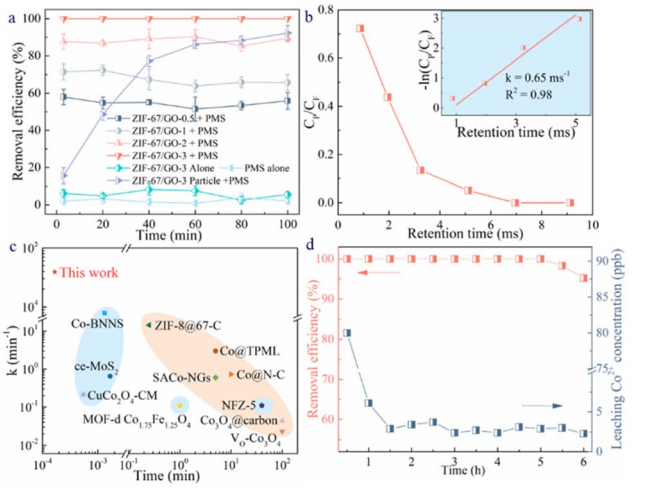

Fig. 2 (a) The degradation efficiency of BPA in different reaction systems. (b) BPA concentration ($C_{permeate}/C_{feed}$) *versus* membrane retention time in the ZIF-67/GO-3 membrane/PMS system. The inset shows the first-order kinetics. (c) Comparison of the ZIF-67/GO-3 membrane/PMS system with previously developed catalytic membranes. (d) Stability test and Co^{2+} leaching of the ZIF-67/GO-3 membrane/PMS system as a function of reaction time. Reaction conditions: [BPA] = 5 mg L^{-1}, [PMS] = 200 ppm, and pH 10.4.

These results unveiled that designing the nanoconfined ZIF-67/GO-*x* membrane could dramatically improve catalytic performance compared to the common catalytic systems.

In addition, the ZIF-67/GO-3 membrane/PMS system exhibited a higher BPA degradation efficiency than ZIF-67/GO-2 (~87.6%), ZIF-67/GO-1 (~71.5%), and ZIF-67/GO-0.5 (~58.0%) membrane/PMS systems. As shown in the SEM images in Fig. S2b–e,† with a longer synthesis time, more ZIF-67 particles were embedded onto the surface of GO nanosheets, providing an ideal platform for the reaction between the target organic compounds and reactive oxidative species (ultrashort lifetime of 10^{-9} to 10^{-6} s). Therefore, ultrahigh BPA degradation efficiency could be obtained.

The stability of the ZIF-67/GO-3 membrane/PMS system was further explored through a continuous flow experiment. The removal efficiency (Fig. S2d†) and flux (Fig. S7†) remained nearly steady even after 6 h. Metal ion leaching of the PMS activator was conducted as well to evaluate the stability of ZIF-67/GO-3. The leaching amount of Co ions was found to be ~80 μg L^{-1} in the first half hour and remained nearly <10 μg L^{-1} thereafter, which is much lower than the World Health Organization (WHO) guideline value (100 μg L^{-1}) for drinking water quality. For the effect of the same amount of maximum leached cobalt ions (80 μg L^{-1}, ZIF-67/GO-3, Fig. S8†), only <2% BPA could be degraded with homogeneous PMS activation, indicating that BPA was mainly degraded by the heterogeneous catalysis of the ZIF-67/GO-3 membrane, rather than the tiny amount of leached Co^{2+}. Besides, the XPS analysis of the ZIF-67/GO-3 membrane before and after the reactions (Fig. S9†) was conducted to evaluate the chemical stability as well. Only 2.83% of Co(II) was converted into Co(III) after a 6 h reaction (Table S3†), which further demonstrated the excellent stability of the membrane.

To explore the general applicability of the developed ZIF-67/GO-3 membrane-based nanoconfined catalysis, the degradation performance of five other organic pollutants was investigated. Fig. S10† shows the removal efficiencies of different concentrations of BPA and other pollutants, PMS. All pollutants with 5 ppm, including tetracycline, phenol, methylene blue, methyl orange, and congo red, could be rapidly removed with 100% removal efficiencies between 6.8 and 8.3 ms. Table S2† shows the comparison of different kinetics for different pollutants. Therefore, it can be concluded that the ZIF-67/GO-3 membrane is an excellent platform for ultrafast removal of diverse organic pollutants from wastewater.

ROS generation

According to the analysis above, the generation of reactive species aroused by PMS activation played a decisive role in BPA degradation in the ZIF-67/GO membrane/PMS system. As such, the quenching tests were systematically explored in terms of hydroxyl radicals (•OH), sulfate radicals ($SO_4^{\bullet-}$), superoxide radicals ($O_2^{\bullet-}$), and singlet oxygen ($^1O_2$), which may be present in the PMS-based oxidation process.[29] First, both MeOH ($k_{SO_4^{\bullet-}} = 2.5 \times 10^7$ M^{-1} s^{-1}, $k_{\bullet OH} = 9.7 \times 10^8$ M^{-1} s^{-1}) and TBA ($k_{SO_4^{\bullet-}} = 4$–9.5×10^5 M^{-1} s^{-1}, $k_{\bullet OH} = 3.8$–7.6×10^8 M^{-1} s^{-1}) worked as the scavengers of •OH and $SO_4^{\bullet-}$ radicals due to their excellent second-order reaction rate.[30] A noticeable inhibitory effect could be observed as the BPA degradation efficiency decreased from 100% to 82.15% and 75.84% with 1 M MeOH and TBA, respectively (Fig. 3a). Superoxide radicals ($O_2^{\bullet-}$), another kind of common ROSs in the AOPs, were also examined in this study. However for the scavengers of $O_2^{\bullet-}$, the maximum amount of 500 mM carbonate ($k_{CO_3^{2-}} = 5 \times 10^8$ M^{-1} s^{-1}) and 10 mM BQ ($k_{BQ} = 2.9 \times 10^9$ M^{-1} s^{-1})[31] had nearly no effect on BPA removal (Fig. 3b). Besides, from Fig. S11,† singlet oxygen ($^1O_2$) played a negligible role in the presence of L-His serving as the quenching agent as well. According to the aforementioned result, both •OH and $SO_4^{\bullet-}$ radicals were revealed to play a dominant role in the ZIF-67/GO-3 membrane/PMS system. Although the quenching effect of 1 M MeOH or TBA was not strong enough to significantly decrease the BPA removal efficiency, it might be attributed to the strong oxidizability of this system.

To further ascertain the generation of active species for BPA removal, the quantitative study of •OH and $SO_4^{\bullet-}$ radicals was conducted through the aromatic hydroxylation of terephthalic acid[32] and benzoic acid,[33] respectively. The fluorescence intensity at around 440 nm gradually increased with the synthesis time of the ZIF-67/GO materials (Fig. 3c and S12a†), confirming the generation of •OH radicals. Moreover, the trend of fluorescence intensity was the same as that of the BPA degradation efficiency (Fig. 2a), indicating the involvement of •OH radicals.

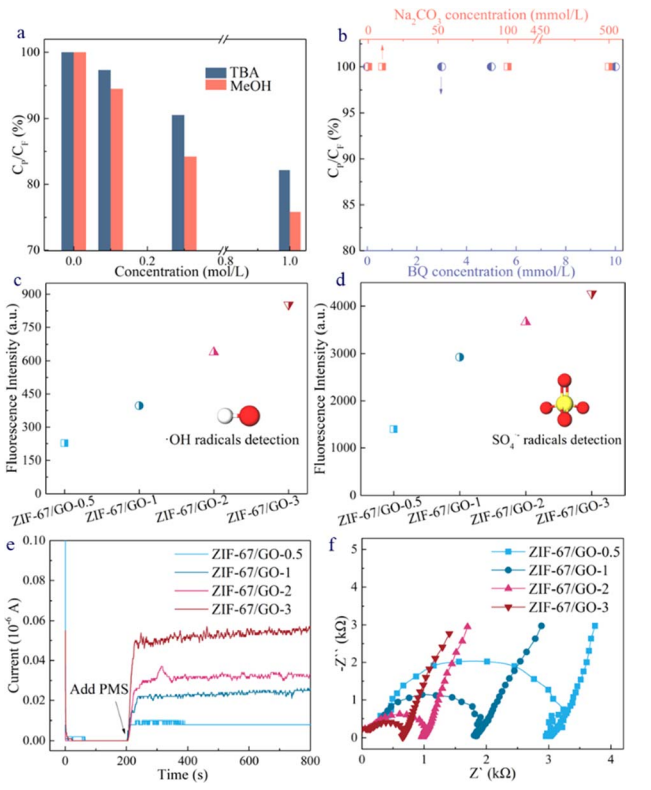

Fig. 3 Quenching test of (a) MeOH, TBA, and (b) BQ, CO_3^{2-} with different concentrations. Generation of (c) hydroxyl radicals (•OH) and (d) sulfate radicals $SO_4^{\bullet-}$. (e) Current–time curve response and (f) Nyquist plots at open circuit potential for different reaction systems. Reaction conditions: [BPA] = 5 mg L^{-1}, [PMS] = 200 ppm, and pH 10.4.

Similarly, based on the fluorescence emission peak at 403 nm (Fig. 3d and S12b†), the production of $SO_4^{\bullet-}$ radicals was also verified in the ZIF-67/GO-*x* membrane/PMS systems, suggesting their contribution to BPA degradation. As one of the main active species, superoxide radicals ($O_2^{\bullet-}$) were also detected here. However, based on the UV spectra of $O_2^{\bullet-}$ in benzoic acid solution, as displayed in Fig. S12c,† there were no peaks at about 259 nm for all the ZIF-67/GO-*x* membrane/PMS systems,[34] demonstrating that there was almost no production of $O_2^{\bullet-}$. These results align with the above quenching test and catalytic performances discussed earlier.

In PMS-activated AOPs, it is well known that the electron transfer efficiency plays a key role in the production efficiency of ROSs.[35] Electrochemical characterization was thus conducted here to explore the electron transfer process. The current–time curves in Fig. 3e exhibited an increasing current response for all the materials when adding the PMS into the electrolyte at 200 s. However, with a longer synthesis time of ZIF-67/GO-*x*, a much higher current response could be achieved, corresponding to the BPA removal and ROS generation trends. This result confirmed the superior electron transfer efficiency of ZIF-67/GO-3 compared to the other three materials when reacting with PMS. Electrochemical impedance spectroscopy (EIS) was also employed to compare the electron transfer capacity of these materials at the same potential. It was obvious that ZIF-67/GO-3 showed the smallest semicircle diameter compared to the other three materials. The semicircle diameter became larger with the decrease of synthesis time, indicating that ZIF-67/GO-3 got the smallest electron transfer resistance among them. It was concluded that the electron transfer process occurred more easily between catalysts and PMS molecules in the ZIF-67/GO-3 membrane/PMS system, resulting in the generation of more active species for BPA degradation.

It is well known that effective PMS activation is mainly caused by efficient redox recycling of polyvalent metals between M^{n+1} and M^{n+}. Due to the denser active sites of ZIF-67/GO-3, more redox reactions may occur in the ZIF-67/GO-3 membrane/PMS system, leading to more electron transfer processes. From the above analysis of XPS and ROS detections, the generation pathways of $^{\bullet}OH$ and $SO_4^{\bullet-}$ radicals were proposed with the redox recycle of Co^{2+}/Co^{3+} as follows:[36–38]

$$Co^{2+}@ZIF\text{-}67 + HSO_5^- \rightarrow Co^{3+}@ZIF\text{-}67 + SO_4^{\bullet-} + OH^- \quad (1)$$

$$SO_4^{\bullet-} + H_2O \rightarrow SO_4^{2-} + {}^{\bullet}OH + H^+ \quad (2)$$

$$Co^{3+}@ZIF\text{-}67 + HSO_5^- \rightarrow Co^{2+}@ZIF\text{-}67 + SO_5^{\bullet-} + H^+ \quad (3)$$

$$2SO_5^{\bullet-} \rightarrow 2SO_4^{\bullet-} + O_2 \quad (4)$$

$$SO_5^{\bullet-} + 2H_2O \rightarrow SO_4^{2-} + 3{}^{\bullet}OH + H^+ \quad (5)$$

$$SO_4^{\bullet-} \text{ and } {}^{\bullet}OH + BPA \rightarrow \text{intermediates} \rightarrow CO_2 + H_2O \quad (6)$$

Specifically, Co^{2+} on the ZIF-67 framework was oxidized to Co^{3+} by activating HSO_5^-, accompanied by the generation of $SO_4^{\bullet-}$ radicals (eqn (1)). $^{\bullet}OH$ radicals were then produced by the activation of water caused by $SO_4^{\bullet-}$ radicals (eqn (2)). Subsequently, Co^{3+} was reduced to Co^{2+} through the reaction with the HSO_5^- group to generate $SO_5^{\bullet-}$ radicals, realizing a redox cycle (eqn (3)). The $SO_5^{\bullet-}$ radicals immediately reduced to $SO_4^{\bullet-}$ radicals and reacted with water to generate $^{\bullet}OH$ radicals (eqn (4) and (5)). With the maximum exposure of active sites and edges in the ZIF-67/GO membrane, high yields and effective utilization of active radicals were realized through the low mass transfer resistance. $SO_4^{\bullet-}$ and $^{\bullet}OH$ radicals play the most important roles in BPA degradation (eqn (6)).

BPA degradation intermediates

Besides analyzing ROS generation and electron transfer processes, the BPA degradation pathway was explored in the nanofluidic platform. Liquid chromatography-mass spectrometry (LC-MS) spectra were recorded to analyze intermediates (Table S4†) after the permeation through the ZIF-67/GO-3 membrane with different concentrations of PMS. As illustrated in Fig. 4a, *m*/*z* 227.1 represented BPA, which could be broken down by the ZIF-67/GO membrane when the PMS concentration reached 200 ppm, consistent with the PMS optimization outcome (Fig. S5b†). At the beginning of the reaction, hydroxylated byproducts of *m*/*z* 241.1, 255.2, and 275.0 were identified in LC-MS spectra with 20–100 ppm PMS (Fig. 4a).

Two plausible pathways for this process include the generation of a radical cation (BPA^+) from the electron transfer of $SO_4^{\bullet-}$ and the electrophilic attack of $^{\bullet}OH$ radicals (Fig. 4b).[39] Compared to nonselective $^{\bullet}OH$ radicals that can attack either the aromatic ring or aliphatic chain, $SO_4^{\bullet-}$ radicals were more involved in electron transfer processes, attacking the aromatic ring and contributing to the addition and abstraction of hydrogen.[40] Three peaks with *m*/*z* values of 150.9, 152.9, and 259.0 gradually became more pronounced with 200 ppm PMS, indicating the degradation of BPA. The intermediate with *m*/*z* 150.9 involved the scission of the right (R) ring and further oxidation with active radicals to form the hydroxyl group (Fig. 4b). Then the benzene ring was oxidized to form low molecular weight substances, including succinic acid, 1,5-hexadiene-3,4-diol, hydroquinone, *etc.* (Table. S3†). These intermediates were subsequently mineralized to H_2O and CO_2.

BPA degradation pathways inside the ZIF-67/GO membrane

As a characteristic of ZIF-67, its porous structure should also play an important role in BPA degradation. According to the previous studies,[41] theoretically, the largest effective aperture of ZIF-67 windows at room temperature (d_{298k}) can be at most 7.26 Å owing to the well-known framework flexibility (ligand rotation).[16,42] From the side views of PMS (3.15 Å × 3.05 Å×3.5 Å) and BPA (4.01 Å × 4.98 Å × 7.44 Å), as shown in Fig. 5a, they were smaller than the effective apertures of ZIF-67 windows and cavities of 11.4 Å. Hence, PMS and BPA molecules could theoretically enter into the cavity of ZIF-67 and conduct the redox reactions in ZIF-67 pores (Fig. 5b). In addition, smaller molecules of intermediates of BPA, such as succinic acid, 1,5-hexadiene-3,4-diol, and hydroquinone, or active species, might also access the cavities and windows of ZIF-67. The likelihood of entering ZIF-67 cavities for different molecules is shown in

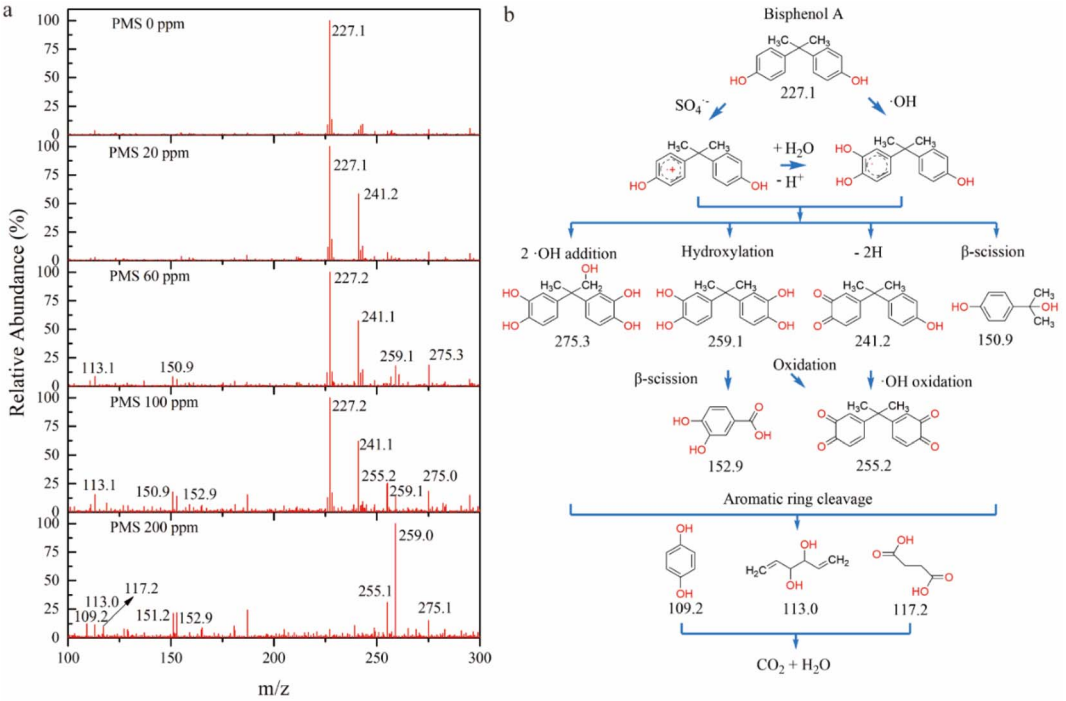

Fig. 4 (a) LC-MS spectra of BPA and its intermediates upon degradation with 0 ppm, 20 ppm, 60 ppm, 100 ppm, and 200 ppm PMS. (b) Proposed BPA degradation pathway with intermediate structures in the ZIF-67/GO-3 membrane/PMS system. The intermediate structures are confirmed from the *m*/*z* values shown in (a).

Fig. S13† based on the different side views. Therefore, most of the BPA and its derived byproducts would pass through the laminar membrane in the easiest and fastest way with less resistance until they are transformed into small molecules such as CO_2 and H_2O. But it could also be speculated that part of the BPA intermediates might be removed by the activation of PMS *via* active catalytic sites inside the ZIF-67 cavities. Therefore, both ZIF-67 pores and interlayer nanochannels within the ZIF-67/GO membranes could function as nanoconfined spaces for PMS activation toward BPA degradation (Fig. 5b).

To test this hypothesis, FTIR analysis was conducted on pure BPA, pure ZIF-67/GO, and ZIF-67/GO + degraded BPA. As shown in Fig. 5c, the absorption band at 418 cm^{-1} indicated the Co–N bond in the ZIF-67 structure. C=N and C=C structures were evident at 1566 and 1608 cm^{-1}, respectively. The peaks at 984 and 1722 cm^{-1} were attributed to the C–N tensile vibration in the ZIF-67/GO nanosheets and C=O bending vibration, respectively. The broad band at 3399 cm^{-1} represented the O–H stretching vibration. Sharp peaks below 800 cm^{-1} could be attributed to the out-of-plane bending while peaks between 900 and 1400 cm^{-1} stood for the in-plane bending of the ring. Nearly all these peaks could be found in the sample ZIF-67/GO + degraded BPA as well even though the sample was washed three times with the buffer solution before the analysis. These peaks in the hybrid sample might come from the intermediates that entered the cavity of ZIF-67 but had not yet been completely degraded. A similar conclusion was drawn from the thermogravimetric analysis (TGA) and their derivative (DGA) curves (Fig. 5d and S14†). The thermal decomposition of BPA began after 250 °C. For ZIF-67 and ZIF-67/GO, a significant weight loss occurred between 420 °C and 580 °C attributed to the decomposition of the crystal structure. It could be also concluded that the weight percentage of GO in ZIF-67/GO was around 2.7%. For ZIF-67/GO + degraded BPA, there was an obvious weight loss before 170 °C. The weight loss before 120°C might come from water desorption and the weight between 120 and 170°C might come from decomposition of small molecule intermediates. A rapid weight loss was observed between 220 °C and 350 °C, resembling the decomposition pattern as shown in the ZIF-67 sample (Fig. S14†), albeit more condensed and occurring more quickly. The loss is likely due to the partial decomposition of the MOF lattice, indicated by the relatively consistent residue ratio observed. This decomposition appears to have been accelerated by peroxide from the PMS adsorbed within the MOF pores, leading to an earlier and more rapid decomposition. According to the above analysis, some phenol with one or two rings may have entered the cavities of ZIF-67, along with smaller molecule byproducts. This conclusion aligns with the proposed BPA degradation pathways. Firstly, most BPA molecules would pass through the confined ZIF-67/GO membrane between the closely embedded ZIF-67 particles due to the low resistance of the flux. Secondly, due to the framework flexibility of ZIF-67, part of the intermediates would enter the cavity of the ZIF-67 cages to form a large amount of local nanoconfined environment. As such, the full use of active sites to generate active radicals both inside and outside the cavity contributed to the high catalytic performance of the ZIF-67/GO membrane/PMS system.

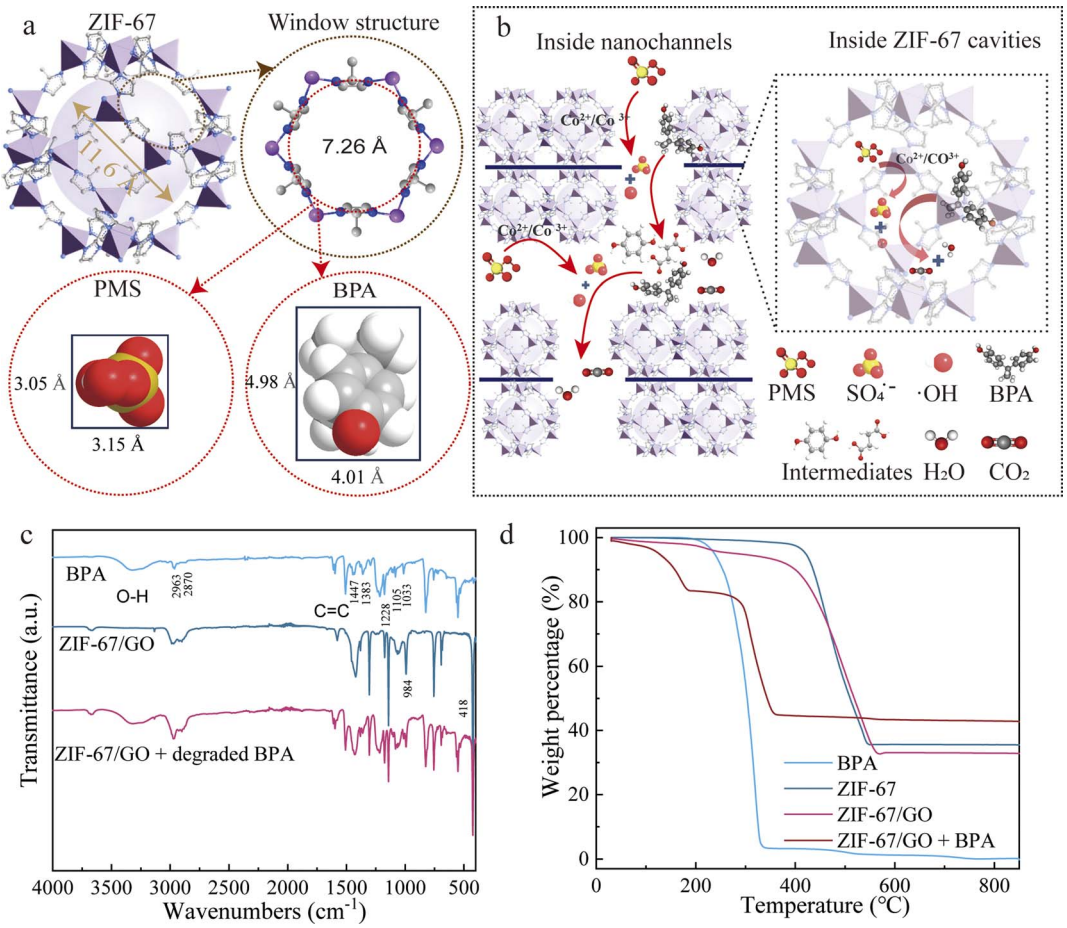

Fig. 5 (a) The effective aperture of the ZIF-67 window and the likelihood of PMS and BPA molecules entering into the cavity of ZIF-67. (b) The degradation process of BPA in both nanochannels of the ZIF-67/GO membrane and cavities of ZIF-67. (c) FTIR spectra of BPA, ZIF-67/GO-3, and ZIF-67/GO-3 with absorbed BPA byproducts. (d) TGA curves of BPA, ZIF-67, ZIF-67/GO, and ZIF-67/GO with absorbed BPA byproducts.

Conclusions

A nanofluidic membrane platform based on ZIF-67/GO nanosheets has been employed to effectively activate PMS under alkaline conditions for organic pollutant degradation. The membrane with a hybrid pore structure consisting of interlayer 2D nanochannels and intrinsic nanopores on the nanosheets exhibited a superior BPA degradation rate of 0.65 ms^{-1} at a high-water flux of 875 L m^{-2} h^{-1} bar^{-1}. By activating PMS within laminar nanochannels between the ZIF-67/GO nanosheets and intrinsic ZIF-67 nanopores, the membrane performance was significantly higher than other current reports by up to four orders of magnitude. The quenching test and chemical probes demonstrated that both $^{\cdot}OH$ and $SO_4^{\cdot-}$ played a predominant role in contaminant removal due to the fast electron transfer efficiency detected through the electrochemical characterization. Notably, based on the FTIR and TGA results, two main degradation routes of BPA molecules in the nanoconfined ZIF-67/GO membrane were identified. One was to pass through nanochannels between the ZIF-67/GO nanosheets and contact the active sites outside ZIF-67 cavities. The other was to enter the interior of the ZIF-67 cavities and contact the active sites inside the ZIF-67 cavities. Both pathways boosted the ROS yields and strengthened mass transfer processes. We anticipate that the nanofluidic membrane platforms with nanoconfined angstrom-porous framework catalysts would provide an effective strategy for alkaline wastewater treatment.

Experimental procedures

Preparation of 2D ZIF-67/GO nanosheets and membranes

Graphene oxide (GO) suspension was fabricated from graphite powder with the modified Hummers' method.[43] Accordingly, 5 mg per mL GO suspension was achieved and was then diluted to 1 mg mL^{-1} by methanol. After 5 h sonication, the final GO suspension was obtained with the solvent of water/methanol mixture (1 : 4, v/v). 145.5 mg $Co(NO_3)_2 \cdot 6H_2O$ and 328.5 mg Hmim were dissolved in 10 mL methanol separately, with stirring 15 min. 5 mL GO suspension and 10 μL TEA were immediately added when the metal ions and organic ligand solution mixed. After x hour stirring ($x = 0.5, 1, 2, 3$), ZIF-67/GO-x could be achieved with centrifugation (10 000 rpm, 5 min) and washed with methanol three times. Then, the resulting paste material

was weighed and diluted with methanol to prepare a 10 mg mL^{-1} suspension.

The ZIF-67/GO-*x* membrane was prepared by direct vacuum filtration of a certain amount (1 mg to 8 mg) of ZIF-67/GO-*x* nanosheets through a porous polyethersulfone (PES) support membrane with a mean pore size of 0.03 μm and 13 mm diameter, which was provided by Sterlitech Corporation (USA).

Material characterization and analytical methods

The morphology and the size of the nanosheets were analyzed by scanning electron microscopy (SEM, FEI Verios 460L SEM). Powder X-ray diffraction (XRD, D4 Endeavour, Bruker) with Cu Kα radiation ($\lambda = 1.5418$ Å) was used to characterize the crystalline structure of the fabricated materials. The Brunauer–Emmett–Teller method (BET, Micromeritics ASAP 2460) was employed to analyze the specific surface area. The thermogravimetric analysis (TGA) was conducted with the analyzer TGA 8000 with Autosampler PerkinElmer, at a heating rate of 10 °C min^{-1} from 30 to 850 °C with an air flow of 20 mL min^{-1}. X-ray photoelectron spectroscopy (XPS) analysis (Thermo Scientific K-Alpha XPS) was utilized to analyze the elemental compositions and the valence states of constituent elements with an Al Kα radiation source. The surface properties of the samples were analyzed by Fourier transform infrared spectroscopy (FTIR, FT-IR/FIR Spectrometer Frontier, PerkinElmer).

Detection of active radicals

Active radicals, including hydroxyl radicals (•OH) and sulfate radicals ($SO_4^{\bullet -}$), were detected with terephthalic acid[32] and benzoic acid[29] solution serving as the probes, respectively, using the fluorescence method (Spectrofluorometer, FluoroMax-4, Horiba). Superoxide radicals ($O_2^{\bullet -}$) were detected with probes of nitro blue tetrazolium (NBT)[44] solution using the UV spectrophotometric (Series UV-Vis-NIR Spectrophotometer, Agilent) spectral method.

Electrochemical characterization methods, including the current–time curve response and Nyquist plots at open circuit potential, were carried out using an electrochemical station (Vertex, Ivium Technologies). A saturated Ag/AgCl electrode and a platinum rod served as the reference and counter electrodes, respectively. Fluorine-doped Tin Oxide (FTO) glass (1 × 2 cm, OPV Tech Co., Ltd, China) was used as the working electrode coating the ZIF-67/GO nanosheets (100 μL, 100 mg L^{-1}) 3 times. The electrode was dried in an oven at 80 °C for 10 min after each coating. 0.2 M Na_2SO_4 served as the electrolyte.

Conflicts of interest

There are no conflicts to declare.

Acknowledgements

This work was supported by the Australian Research Council (FT200100259 and DE220100435). The authors acknowledge and appreciate the usage of facilities and assistance from RMIT Microscopy and Microanalysis Facility (RMMF) for materials characterization. Dr Jian Hu appreciated the facilities and technical support from RMIT Analytical Chemistry for the catalytic performance test.

Notes and references

1 L. Wu, B. Li, Y. Li, X. Fan, F. Zhang, G. Zhang, Q. Xia and W. Peng, *ACS Catal.*, 2021, **11**, 5532–5543.
2 M. Li, S. You, X. Duan and Y. Liu, *Appl. Catal., B*, 2022, **312**, 121419.
3 S. Wang, T. Li, X. Cheng, R. Zhu and Y. Xu, *Water Res.*, 2023, **233**, 119744.
4 T. Yu, H. Chen, T. Hu, J. Feng, W. Xing, L. Tang and W. Tang, *Appl. Catal., B*, 2024, **342**, 123401.
5 X. Huang, T. Shen, T. Zhang, H. Qiu, X. Gu, Z. Ali and Y. Hou, *Adv. Energy Mater.*, 2019, **10**, 1900375.
6 Q. Zhu, Q. Xu, M. Du, X. Zeng, G. Zhong, B. Qiu and J. Zhang, *Adv. Mater.*, 2022, **34**, e2202929.
7 S. Qu, Y. Yuan, X. Yang, H. Xu, A. K. Mohamed, J. Zhang, C. Zhao, L. Liu, B. Wang, X. Wang, J. Rinklebe, Y. C. Li and S. Wang, *Chem. Eng. J.*, 2022, **441**, 135864.
8 Y. Bao, C. Lian, K. Huang, H. Yu, W. Liu, J. Zhang and M. Xing, *Angew. Chem., Int. Ed.*, 2022, **61**, e202209542.
9 Y. J. Zhang, G. X. Huang, L. R. Winter, J. J. Chen, L. Tian, S. C. Mei, Z. Zhang, F. Chen, Z. Y. Guo, R. Ji, Y. Z. You, W. W. Li, X. W. Liu, H. Q. Yu and M. Elimelech, *Nat. Commun.*, 2022, **13**, 3005.
10 Z. Wang, E. Almatrafi, H. Wang, H. Qin, W. Wang, L. Du, S. Chen, G. Zeng and P. Xu, *Angew. Chem., Int. Ed.*, 2022, **61**, e202202338.
11 T. Liu, S. Xiao, N. Li, J. Chen, X. Zhou, Y. Qian, C. H. Huang and Y. Zhang, *Nat. Commun.*, 2023, **14**, 2881.
12 L. Zhang, J. Qi, W. Chen, X. Yang, Z. Fang, J. Li, X. Li, S. Lu and L. Wang, *Environ. Sci. Technol.*, 2023, **57**, 16141–16151.
13 W. Zhang, S. Zhang, C. Meng and Z. Zhang, *Appl. Catal., B*, 2023, **322**, 122098.
14 G. Wang, K. Wang, Z. Liu, Y. Feng, S. Yang, Y. Su, X. Qian, P. Jin and J. Wei, *Appl. Catal., B*, 2023, **325**, 122359.
15 Y. Ma, Y. Meng, Z. Wang, Y. Xin, X. Lv, Q. Li, H. Wang, H. Xie and Z. Zhang, *Chem. Eng. J.*, 2023, **476**, 146694.
16 Y. Hu, J. Wei, Y. Liang, H. Zhang, X. Zhang, W. Shen and H. Wang, *Angew. Chem., Int. Ed.*, 2016, **55**, 2048–2052.
17 H. Li, Z. Yang, S. Lu, L. Su, C. Wang, J. Huang, J. Zhou, J. Tang and M. Huang, *Chemosphere*, 2021, **273**, 129643.
18 W. Mei, D. Li, H. Xu, J. Zan, L. Sun, Q. Li, B. Zhang, Y. Wang and D. Xia, *Chem. Phys. Lett.*, 2018, **706**, 694–701.
19 N. Li, G. Chen, J. Zhao, B. Yan, Z. Cheng, L. Meng and V. Chen, *J. Membr. Sci.*, 2019, **591**, 117341.
20 Q. Yang, S. Ren, Q. Zhao, R. Lu, C. Hang, Z. Chen and H. Zheng, *Chem. Eng. J.*, 2018, **333**, 49–57.
21 H. Zhang, J. Hou, Y. Hu, P. Wang, R. Ou, L. Jiang, J. Z. Liu, B. D. Freeman, A. J. Hill and H. Wang, *Sci. Adv.*, 2018, **4**(2), eaaq0066.
22 J. Wei, Y. Hu, Z. Wu, Y. Liang, S. Leong, B. Kong, X. Zhang, D. Zhao, G. P. Simon and H. Wang, *J. Mater. Chem. A*, 2015, **3**, 16867–16873.

23 W. Shao, C. He, M. Zhou, C. Yang, Y. Gao, S. Li, L. Ma, L. Qiu, C. Cheng and C. Zhao, *J. Mater. Chem. A*, 2020, **8**, 3168–3179.
24 M. Kohantorabi, S. Giannakis, G. Moussavi, M. Bensimon, M. R. Gholami and C. Pulgarin, *J. Hazard. Mater.*, 2021, **413**, 125308.
25 K.-Y. Andrew Lin, F.-K. Hsu and W.-D. Lee, *J. Mater. Chem. A*, 2015, **3**, 9480–9490.
26 L. Ding, Y. Wei, Y. Wang, H. Chen, J. Caro and H. Wang, *Angew. Chem., Int. Ed.*, 2017, **56**, 1825–1829.
27 B. Li, Y. F. Wang, L. Zhang and H. Y. Xu, *Chemosphere*, 2022, **291**, 132954.
28 J. Lee, U. von Gunten and J. H. Kim, *Environ. Sci. Technol.*, 2020, **54**, 3064–3081.
29 M. Zhang, C. Xiao, X. Yan, S. Chen, C. Wang, R. Luo, J. Qi, X. Sun, L. Wang and J. Li, *Environ. Sci. Technol.*, 2020, **54**, 10289–10300.
30 J. Hu, B. Qian, X. Zeng, Y. Qi, Y. Liu, L. Zhang and X. Zhang, *J. Mater. Chem. A*, 2021, **9**, 16489–16499.
31 J. Hu, X. Zeng, G. Wang, B. Qian, Y. Liu, X. Hu, B. He, L. Zhang and X. Zhang, *Chem. Eng. J.*, 2020, **400**, 1258569.
32 X. Tan, Y. Wan, Y. Huang, C. He, Z. Zhang, Z. He, L. Hu, J. Zeng and D. Shu, *J. Hazard. Mater.*, 2017, **321**, 162–172.
33 P. Hu and M. Long, *Appl. Catal., B*, 2016, **181**, 103–117.
34 M. Li, F. Liu, Z. Ma, W. Liu, J. Liang and M. Tong, *Chem. Eng. J.*, 2019, **371**, 750–758.
35 X. Dong, X. Duan, Z. Sun, X. Zhang, C. Li, S. Yang, B. Ren, S. Zheng and D. D. Dionysiou, *Appl. Catal., B*, 2020, **261**, 118214.
36 X. Li, Z. Ao, J. Liu, H. Sun, A. I. Rykov and J. Wang, *ACS Nano*, 2016, **10**, 11532–11540.
37 S. Zhu, X. Li, J. Kang, X. Duan and S. Wang, *Environ. Sci. Technol.*, 2019, **53**, 307–315.
38 J. Deng, S. Feng, K. Zhang, J. Li, H. Wang, T. Zhang and X. Ma, *Chem. Eng. J.*, 2017, **308**, 505–515.
39 B. Darsinou, Z. Frontistis, M. Antonopoulou, I. Konstantinou and D. Mantzavinos, *Chem. Eng. J.*, 2015, **280**, 623–633.
40 F. Minisci, A. Citterio and C. Giordano, *Acc. Chem. Res.*, 1983, **16**, 27–32.
41 D. M. Polyukhov, A. S. Poryvaev, S. A. Gromilov and M. V. Fedin, *Nano Lett.*, 2019, **19**, 6506–6510.
42 K. Qu, K. Huang, J. Xu, L. Dai, Y. Wang, H. Cao, Y. Xia, Y. Wu, W. Xu, Z. Yao, X. Guo, C. Lian and Z. Xu, *Angew. Chem., Int. Ed.*, 2022, **61**, e202213333.
43 H. Liu, H. Wang and X. Zhang, *Adv. Mater.*, 2015, **27**, 249–254.
44 R. Liu, S. Fu, H. Zhan and L. Lucia, *Ind. Eng. Chem. Res.*, 2009, **48**(20), 9331–9334.